Investigating the Role of PM6:Y7 Layer Thickness on Optimizing Non-Fullerene Organic Solar Cells Performance Through Impedance Spectroscopy Analysis

ENAS MOUSTAFA[ID]**, JOSEP PALLARÈS**[ID]**, AND LLUIS F. MARSAL**[ID] **(Senior Member, IEEE)**

Department of Electronic, Electric and Automatic Engineering, Universitat Rovira i Virgili, 43007 Tarragona, Spain

CORRESPONDING AUTHOR: E. MOUSTAFA (e-mail: enas.moustafa@urv.cat)

ABSTRACT Recently, there has been significant improvement in the power conversion efficiency of non-fullerene organic solar cells, exceeding 19%. In this article, we have fabricated conventional sandwich structure of ITO/PEDOT:PSS/PM6:Y7/PDINO/Ag reaching efficiency up to 17.3% along with high generated current density of 30.60 mA/cm^2 for the optimized devices. The thickness of PM6:Y7 layer has been varied to investigate the impact on the overall device behavior. The obtained results showed that the PCE has been enhanced by 15% upon reducing its thickness from 150 nm to 100 nm. Accordingly, current-voltage measurements and impedance spectroscopy analysis through capacitance-voltage, Mott-Schottky analysis and capacitance frequency under different illumination intensities were conducted to evaluate the behaviour of the charge recombination due to thickness variation of the PM6:Y7 photoactive layer.

INDEX TERMS High efficiency nonfullerene based organic solar cells, impedance spectroscopy, charge carrier recombination mechanism.

I. INTRODUCTION

Third-generation organic solar cells (OSCs) are attractive thanks to their low material consumption, using abundant organic materials, simple solution processability, high absorption coefficient, tunable material properties, and their ability to be highly flexible and transparent [1], [2]. Other advantages include their vocation applications such as indoor light-harvesting technology and wearables electronics [2], [3]. Over two decades, remarkable progress was observed for the development of OSCs that are based on fullerene derivative acceptors in bulk heterojunction (BHJ) structure which considered to meet all these mentioned obligations [4]. In fact, acceptor materials except fullerene derivatives, classified as non-fullerene acceptors (NFA), usually achieved less power conversion efficiency (PCEs), which were mostly due to troubles in handling the

morphology and solution solubility [5], [6]. This scenario has been changed lately where rapid progress obtained in the development of small molecules non-fullerene organic solar cells (NF-OSCs) [7]. The PCEs of the NF-OSCs now are higher than the foremost fullerene-based ones [8], [9]. Configuring low bandgap materials that possessed a fine match with the solar spectrum is an effective strategy for enhancing the generated current and in turn the PCEs of the OSCs [10], [11], [12], [13]. Novel non-fullerene acceptor materials such as Y series, along with novel donor polymers, PM6 (PBDB-T-2F), D16, and D18, have recently broke the barrier of 19% efficiency for a single junction OSCs [8], [14], [15], [16], [17]. The NF-OSCs showed the efficient exciton separation capability with insignificant driving energies achieving enhanced performance in regard to the energy levels of the selected donor counterpart [18], [19].
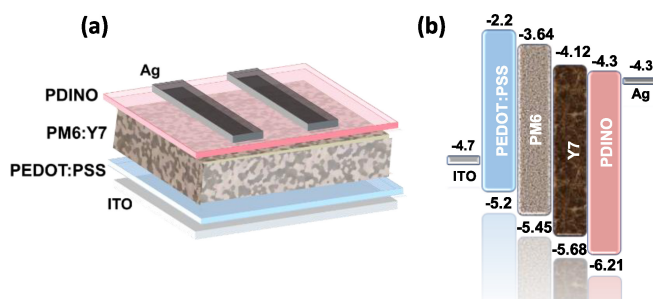
FIGURE 1. (a) The schematic diagram of the NF-OSCs devices structure. (b) the energy level cascade of the device configuration, the energy positions were taken from [15], [35], and [36] references.

In addition, NF acceptors provided an easy tunability of the energy levels with high electron mobility and broad absorption in the near-infrared region (NIR) [20]. As a result, NF-OSCs exhibit the niche advantage of simultaneously demonstrating high generated photocurrent with low voltage losses [21], in contrast to the fullerene counterpart based cells which have trade-off behavior [22], [23], [24]. Furthermore, enhancing the photocurrent and photovoltage of NF-OSCs is a straightforward approach to improve the performance of photovoltaic devices from a device perspective. Hence, the current investigations of photophysics and device performance are mainly due to the great developments of device engineering and materials.

Additionally, it is worth noting the impact of the structure, morphology, and thickness on the performance of NF-OSCs. These effects might cause static disorder creating intrinsic sites of traps in the devices [25]. Therefore, several studies were conducted to tune the microstructure morphology and photoactive film thicknesses of the NF-OSCs [26], [27], [28]. Because it is critical step for the performance improvement of NF-OSC devices due to the large exciton binding energy as well as small exciton diffusion length [26]. Thermal annealing is one of the effective ways to modify the morphology to exhibit an efficient charge separation at the donor/acceptor interface [29], [30], [31]. In addition, the thickness of the active absorber layer for the high efficiency based devices is within 80-300 nm where the PCEs are remarkably decreasing upon increasing the thickness [32], [33], [34].

Accordingly, this study aims to investigate the impact of PM6:Y7 photoactive layer thickness on the performance of organic solar cells. The devices were fabricated with a structure of ITO/PEDOT:PSS/PM6:Y7/PDINO/Ag (**Figure 1a**) with the energy band diagram demonstrated in **Figure 1b**, where PEDOT:PSS served as the hole transport layer (HTL) and PDINO as the electron transport layer (ETL). All the layers were deposited via solution processing using spin coating to precisely control their thickness (see the **II. Experimental Methods** section). The thickness of the interfacial layers (PEDOT:PSS and PDINO) were kept constant to ensure a fair comparison with the varying PM6:Y7 layer thickness. To investigate the electrical properties and

charge recombination dynamics, various characterization techniques such as current density-voltage (J-V) measurements, impedance spectroscopy (IS) using capacitance-voltage (CV) and capacitance-frequency (Cf) analysis were conducted under different illumination intensities (10, 16, 25, 50, 80, and 100 mW/cm^2). The results of this study provide a comprehensive understanding of the correlation between the PM6:Y7 layer thickness and the performance of organic solar cells.

II. EXPERIMENTAL METHODS

This section describes the materials, synthesis procedures and the characterization tools utilized during the fabrication and investigation of the conventional NF-OSCs based on a structure of ITO/PEDOT:PSS/ PM6:Y7/ PDINO/Ag.

Materials: The indium tin oxide (ITO) substrate was supplied from PsiOTec. PDINO employed as ETL, the donor polymer PM6 (PBDB-T-2F) and the non-fullerene acceptor Y7 (BTP-4Cl) were purchased from One-Material. PEDOT: PSS aqueous solution used as HTL was delivered from Clevios P VP Al 4083 from H.C.Starck and the 99.999% purity Ag from Testbourne Ltd. The methanol, chlorobenzene (CB) and chloronapthelene (CN) solvents were purchased from sigma Aldrich.

Device Fabrication: Patterned ITOs substrates were cleaned by mixing the detergent and water, which was then subjected to ultrasonication in acetone, methanol, and isopropanol for 10 minutes. The glasses were then placed in an oven at 100 °C for 10 minutes. To remove any organic residue and activate the ITO surface, the glasses were treated with UV-Ozone for 20 minutes. For synthesizing the HTL from PEDOT:PSS aqueous solution, it was filtered by a 0.45 μm filter then spun-coated on the precleaned ITOs. The PEDOT:PSS film was annealed at 150 °C for 10 min, obtaining 30 nm thin layers. 20 mg/ml blend solution of PM6 donor and Y7 NF-acceptor was prepared by dissolving the 1:1 ratio in CB with 0.5 wt % CN additive and stirred for 3 h at 80 °C [30], [37]. Afterward, the stirred solution was filtered and spun-coated over the preheated PEDOT:PSS layer at 1200, 1500, 1600, 1800 and 2000 rpm obtaining films with thicknesses of 150 nm (D1), 100 nm (D2), 95 nm (D3), 80 nm (D4), and 70 nm (D5). Then the PM6:Y7 deposited film was left to anneal at 90 °C for 5 min [38]. The PDINO solutions were prepared with 1.0 mg/ml dissolved in methanol, then filtered and spun coated to form 10 nm thin films. Finally, 100 nm of Ag top contact was deposited via thermal evaporation under high vacuum conditions ($\leq 1 \times 10^{-6}$ mbar) using a shadow mask with a device active area of 0.09 cm^2. It is noteworthy that all deposition steps were performed in a glove box under a nitrogen environment of 99.999% electronic grade N2 (with H$_2$O and O$_2$ concentrations both < 0.1 ppm).

Device Characterization: The thickness of the films prepared (as detailed in **Table 1**) was measured using a surface profilometer (AMBIOS TECHNOLOGY-XP-1). J-V curves (Current density-voltage) and the device parameters were

TABLE 1. The thickness of each layer within the NF-OSCs based devices.

Device	PM6:Y7	PDEOT:PSS	PDINO
D1	150 nm		
D2	100 nm		
D3	95 nm	30 nm	10 nm
D4	80 nm		
D5	70 nm		

TABLE 2. Main performance parameters of the fabricated devices with variable thicknesses of the PM6:Y7 layer.

Device	V_{OC} (V)	J_{SC} (mA/cm^2)	FF (%)	PCE (%)	R_S ($\Omega.cm^2$)	R_{Sh} ($\Omega.cm^2$)
D1	0.81	31.56	58.85	15.04	0.94	315
	0.80±0.1	29.69±1.87	60.36±1.51	14.20±0.84	0.81±0.13	305±10
D2	0.84	30.60	67.40	17.33	0.69	508
	0.84±0.01	30.63±0.08	65.55±1.85	16.78±0.55	0.71±0.08	465±43
D3	0.85	30.04	66.85	17.07	0.76	403
	0.85±0.01	30.12±0.66	66.75±0.10	16.30±0.77	1.14±0.42	398±30
D4	0.83	30.88	64.09	16.425	0.72	389
	0.83±0.01	30.78±0.37	62.95±1.27	16.08±0.43	0.71±0.08	380±20
D5	0.83	30.34	63.83	16.08	0.78	350
	0.83±0.01	30.96±0.53	64.34±0.52	15.82±0.26	0.68±0.21	348±32

The entire devices were measured under 100 mW/cm^2 simulator irradiation at AM 1.5G and the average parameters were calculated from minimum of 9 fabricated devices for each configuration.

measured using Keithley 2400 source-measure unit conjugated with solar simulator system (model 11000 class AAA, Xenon arc lamp) at room temperature, under illumination and dark condition. To obtain a 100 mW/cm^2 and AM1.5 spectrum, a Fraunhofer certified photovoltaic cell was utilized to calibrate the intensity of the solar simulator. Moreover, the V_{OC} and J_{SC} measured versus different light intensities performed by J-V measurements under the solar simulator utilizing optical density filters. Mask with well-defined area was used to specify the effective area for accurate measurement. External quantum efficiency (EQE) measurements were conducted in the wavelength range from 300 nm to 900 nm using Lasing, S.A. (IPCE-DC, LS1109-232) and a Newport 2936-R power-meter unit system. Impedance spectroscopy Analysis (Impedance spectroscopy analysis was accomplished under AM 1.5G illumination conditions, using an AC signal with 50 mV amplitude and frequency range of 5 Hz - 1 MHz, at various applied bias voltages (0.0 V, 0.2 V, V_{mpp}, and V_{OC}), with a HP-4192A impedance analyzer. The same illumination conditions was conducted to the C-V characteristics. The Cf measurements were performed at 1 MHz with the voltage range of −1 to 1 V. It is worth noting that the efficiency of the devices was consistence after the C–V and Cf measurements.

III. RESULTS AND DISCUSSIONS

During the optimization of the NF-OSC device performances, we conducted five different thicknesses of PM6:Y7 absorber photoactive layer as aforementioned in **Table 1**. To simplify the discussion we named each PM6:Y7 layer thickness as following: 150 nm based devices as D1, 100 nm as D2, 95 nm as D3, 80 nm (D4), and 70 nm (D5). The detailed device performance parameters and statistical data of each configuration are illustrated in **Table 2**.

Figure 2a reveals the current density-voltage (J-V) characteristics for the five representative devices (Device 1-Device 5) with various PM6:Y7 photo-absorber layer thicknesses, as aforestated, under illumination conditions. The results depicted that the 100 nm photoactive layer thickness -D2- based devices possessed the highest performance parameters of FF, R_{Sh}, and PCE with 67.40%, 508 $\Omega.cm^2$, and 17.33%, respectively, which quite well consistent with

the reported literatures [15], [16]. In contrast to the D1 (150 nm) based devices that showed the lowest values of V_{OC} = 0.81 V, FF = 58.58%, R_{Sh} = 315 $\Omega.cm^2$ and PCE = 15.04%. By increasing the absorber film thickness from 70 nm to 100 nm, obvious increase in FF was improved from 63.83% for D5, to 64.09% for D4, to 66.85% for D3 and 67.40 for D2, which in turn improves the overall efficiencies of the corresponding devices to 16.08%, 16.43%, 17.07%, and 17.33%, respectively as demonstrated in **Figure 2c** and listed in **Table 2**. This exhibited results are consistence with the reported results by Yuan et al. and Zhan et al. [33], [39]. Hence, this behavior could be ascribed to the diminishing of the series resistance (R_S) along with the increment of R_{Sh}, providing better FF corresponding devices [40]. While the drop of FF in Device 1 might be assigned to increased bulk recombination sites upon higher PM6:Y7 thickness, resulting in a noticeable decline in the R_{Sh} values [41]. Interestingly, the J_{SC} and V_{OC} values showed insignificant influence upon the photoactive layer thickness increment till 100 nm that is barely changed as demonstrated in **Figure 2d**, which matched with the work presented by Cui et al. and Tokmoldin et al. [15], [41]. In contrast to D1-150 nm-based devices, where the J_{SC} along with the R_S increased and the V_{OC} reduced as listed in **Table 2**. The increase in J_{SC} can be explained by the fact that increasing the thickness of the photoactive layer leads to greater absorption and subsequently, an increase in the total number of charges created within the active layer. However, as the thickness of the photoactive layer increases, the photogenerated electrons and holes must move a larger distance to achieve their respective electrodes. Given a constant recombination lifetime, the charges are more likely to recombine before reaching their respective electrodes. Therefore, it can be expected that the photocurrent will increase with the thickness of the photoactive layer due to greater charge generation, unless it is limited by higher recombination [42], [43] that mainly affect the J_{SC}, FF, V_{OC}, and in turn the PCE as obtained in D1 based devices. Furthermore, this phenomenon can explain the bit lower J_{SC} value observed in D3 based devices as compared to the D4 and D5 ones. Thus, adjusting the processing
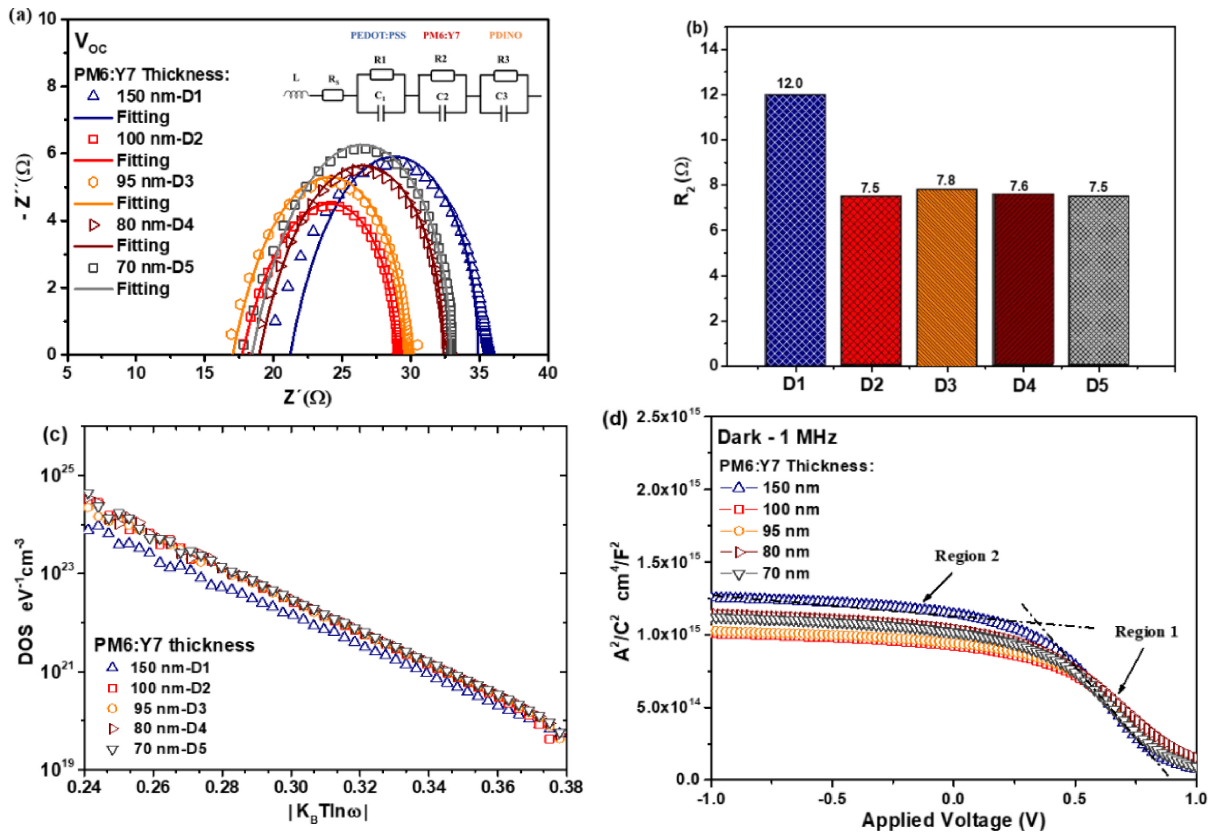
FIGURE 2. J-V characteristic of the NF OSCs fabricated with various thicknesses of PM6:Y7 (a) under Illumination (AM 1.5G), (b) at dark. Devices performance parameters optimization of (c) FF (left) and PCE (right), (d) V_{OC} (left) and J_{SC} (right). (e) The lines are only for eyes guide. J_{Ph} versus V_{eff} characteristics of the NF-OSCs devices.

parameters to increase the film thickness can enhance the value of J_{SC}. However, this may result in a simultaneous decrease in FF, which ultimately fails to improve PCE or even leads to a lower PCE performance [44], [45]. This behaviour was further confirmed by the J-V characteristics under dark condition presented in **Figure 2b**. First, it showed that the significant shunt behaviour was obtained from the thicker absorber active layer in D1 (150 nm) as compared to the others [46], [47]. Second, the D4 and D5 based devices (Thinnest) exhibited lower R_{Sh} values as compared to D2 and D3. This might elucidate the lower values of the FF and V_{OC}. In contrast, the D2 and D3 based ones demonstrate the lowest dark current density and highest V_{OC} and FF values, reflecting the reduced recombination with less voltage losses as will be discussed in detail in the impedance spectroscopy sections [46], [47], [48]. **Figure S1** illustrates the external quantum efficiency (EQE) spectra of the devices based on different photoactive layer thicknesses. The results indicate that increasing the thickness of the absorber active layer only marginally enhances the EQE response in all devices. Moreover, all devices exhibit a similar absorption wavelength range spanning from 300 nm to 900 nm, with an average plateau of approximately 80% and a peak value of 86% at 540 nm for the D1 (150 nm) based devices. Additionally, the integrated J_{SC} values obtained from the EQE spectra are 28.99, 30.04, 29.50,

30.00, and 29.67 mA/cm^2 which in good agreement with the J_{SC} values measured by J-V under illumination with 10% deviation (**Table 2**).

Moreover, the charge generation and exciton dissociation behavior of the fabricated NF-OSCs with varying active layer thicknesses was evaluated by calculating the dependence of photocurrent (J_{Ph}) on effective voltage (V_{eff}). J_{Ph} represents the disparity between light and dark current density. V_{eff} is defined as $V_O - V$, where V_O is the voltage at which J_{Ph} equals zero, and V denotes the applied voltage [49], [50]. The obtained results in **Figure 2e** exhibited that the J_{Ph} increased at low V_{eff} and then came to the saturation of the current density (J_{Sat}) by increasing the V_{eff}. Regarding to this attitude, indicating the efficient photogenerated excitons that dissociated into free carriers and successfully collected by the respective electrodes [51]. As a sequence, the probability of the exciton dissociation ($P_{diss}= J_{SC}/J_{Sat}$) which was > 90% for the entire fabricated devices, revealing the efficient exciton dissociation, charge transport, and charge collection in corresponding NF-OSCs [46], [51]. Despite, there was not much difference between the attitude of the NF-OSCs fabricated in the displayed curves in **Figure 2e** but, it is worth noting that the same interpretation of showing the best behavior obtained from D2 at low V_{eff} (in contrast to D1) which in a good agreement with the high vales of FF, V_{OC} and PCE in D2 more than others.
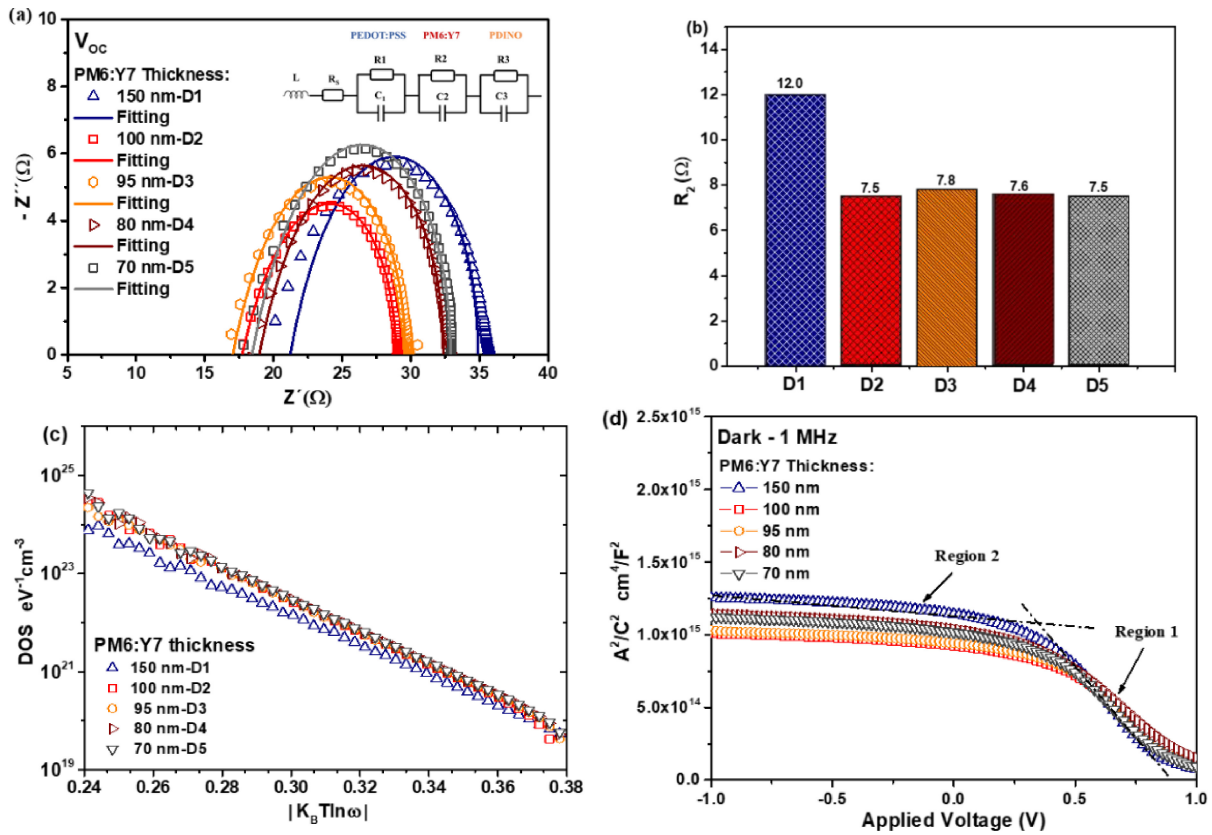
FIGURE 3. (a) Cole-Cole curves at V_{OC}, the experimental data are presented in symbols and the solid lines for the fitting results via applying the 3RC model equivalent circuit in the inset of the figure, (b) The resistance values of the PM6:Y7 layer of each device, extracted from the equivalent circuit 3RC model (c) DOS as function of $|k_BTln\omega|$ at V_{OC} (d) Mott Schottky plot under dark of different thicknesses of the PM6:Y7 active layer of the fabricated NF-OSCs, D1-150 nm, D2-100 nm, D3-95 nm, D4- 80 nm, and D5-70 nm.

Then, to investigate the electric properties of the fabricated devices in terms of interfacial charge transfer and carrier recombination, impedance spectroscopy (IS) was conducted under AM 1.5G illumination conditions [52], [53]. This study also provided insight into the mechanisms underlying performance changes upon varying the thickness of the active layer. **Figure 3a** shows a typical semicircle behavior of Cole-Cole plot of the NF-OSCs based on different PM6:Y7 layer thickness at V_{OC} bias voltage, confirming the efficient active layer/electrode interface transfer [52], [54]. Moreover, It is well known that the size of the arc is mainly representing the device resistance [52]. We noticed that D2 showed the smallest arc radius among the other devices. Moreover, the same behavior was recorded for the entire devices at 0.0 V, 0.2 V and 0.5 V applied bias voltages (Figure **S2**). Then, we fit the experimental Z′-Z″ data via an electrical equivalent circuit to further understanding the devices behaviour. The electrical element employed to fit the plot illustrated in the inset of **Figure 3a** (solid lines) and the extracted fitted parameters were listed in **Table S1**.

The equivalent circuit employed for the impedance spectroscopy comprises of resistive and capacitive (RC) elements, where the resistance of electron transportation in each layer is represented by distributed resistors R1, R2, and R3 correspond to the PEDOT:PSS, PM6:Y7, and the PDINO layer, respectively, reflecting the charge transfer of each layer within the device and the overall collection behaviour. Additionally, C represents the geometrical capacitance values of each layer, indicating a parallel combination of resistor and capacitor for three RC elements in series. R_S signifies the series resistance from the ITO layer and the interface between the ITO and the HTL, while L is an additional inductor included to fit the data at high frequency [52], [54].

The results were interpreted using the fitted data, and it is worth noting that the capacitance values for each layer in the device were consistent with the theoretical values (calculated using Equation (S1) and **Table S2**, and then listed in **Table S3** in the supplementary information), indicating the presence of fully depleted layers [41], [55]. Furthermore, the R_S and R1 values were almost the same in all device which gave an idea that the interfaces between the PEDOT:PSS layer and the PM6:Y7 layer might not affected by changing the thickness of the active layer [56]. In the case of R3 values in all devices which represent the PDINO layer, there was negligible variation observed. The most significant change was related to R2 of the PM6:Y7 layers due to the thickness variation. It showed that D1 possesses the highest R2 value

as displayed in **Figure 3b** that might be a reason of showing the largest radius in **Figure 3a**. Furthermore, in contrast to D1, D2 based devices exhibited the smallest arc radius as well as frequency arc, describing the less pronounced charge accumulation impact as compared to the other devices [27]. Therefore, this behaviour reveals that D2 based devices possessed the lowest device resistance that efficiently assist the charge transfer and collection, resulting in better device performance. Interestingly, this behavior confirms the lowest R_S value observed by D2 based devices in the previously discussed J-V analysis under same condition (**Table 2**).

The IS technique can also be used to understand the recombination mechanisms by measuring the capacitance-frequency (Cf) and calculating the trap density of state (DOS). It is commonly understood that, when trap densities are high, charge carriers that are trapped can still contribute to the overall transport by hopping thermally or tunneling (in the case of shallow traps). However, deep traps serve as recombination centers that are hard to excite, leading to a loss of charges [25]. This measurements were conducted for OSCs mainly to observe the trap emission and disorder-induced within the organic systems [25], [52], [57], [58], [59]. Therefore, to determine the DOS of traps at a specific energy level, E_ω, the capacitance of the device can be varied with frequency. This method is effective for measuring the DOS of shallow traps located in the band gap close to the Fermi energy level, as defined by the equation. (1) [25], [59]

$$\text{DOS}(E_\omega)_{\text{traps}} = -\frac{V_{Bi}\omega}{t\ q\ T\ k_B}\frac{\partial\ C}{\partial\ \omega} \qquad (1)$$

where, C is the capacitance, ω angular frequency, T is room temperature (300K), t layer thickness, V_{Bi} is the built-in voltage, k_B is the Boltzmann constant, and q is the electron charge.

To consider the trap-DOS as an energy dependent, the following equation was applied:

$$(E_\omega)_{\text{traps}} = k_B\ \text{T}\ \ln\frac{2\beta N}{\omega} = E_O - k_BT\ln\omega \qquad (2)$$

where, β is the cross section and N is the effective density of state [23], [60]. Since the value of $2\beta N$ does not depend on the frequency, then the change in its value is correlated to the change in the DOS values with energy scale (E_O).

The trap density of states (DOS) for the cells is shown in **Figure 3c**, which illustrates how the E_O value changes with energy. This behavior can be explained using Equation (2), where the D2 devices had a trap DOS that was one order of magnitude higher than the D1 devices, indicating fewer localized defects in the D2 devices compared to D1 [25], [60], [61], [62]. This behavior was interestingly confirming the lower performance of D1 with deep sight.

Furthermore, **Figure 3d** describes the Mott-Schottky plot of the capacitance-voltage (C-V) data obtained from measurements performed in the dark at a frequency of 1 MHz

for NF-OSCs with various thicknesses of PM6:Y7 films. The graphs for all samples exhibit two distinct regions: region 1, which is linear and ranges from 0.0 V to 1.0 V, corresponds to the contribution from the PM6 donor phase, while region 2, which extends from 0.0 V to −1.0 V, is attributed to the Y7 acceptor phase [59], [63]. We depicted a similar slope of the curves in region 2, while region 1 has showed variable slopes behaviors which indicates the presence of traps effect [59]. So that, to investigate this observed traps sites depending on the PM6:Y7 film thickness variation, the Mott-Schottky analysis was used to evaluate region 1 charge carrier density (N_{PM6}), following equation (3) [41], [59], [63]

$$\left(\frac{A}{C}\right)^2 = \left(\frac{A}{C}\right)^2 = \frac{2(V - V_{Bi})}{q\varepsilon_O\varepsilon_{PM6}N_{PM6}} \qquad (3)$$

where C is the capacitance, A is the photoactive area of the device, V is the applied voltage, q is the elementary charge, V_{Bi} is the built-in voltage, ε_O is the vacuum permittivity, ε_{PM6} is PM6 relative dielectric constant.

Assuming that $N_{Y7} >> N_{PM6}$ (calculated in the SI at **Figure S3a**) and following equation (3) of the C-V analysis under different light intensities (P_{light}) for the devices with different PM6:Y7 film thickness, we then obtained the N_{PM6} vs the P_{light} as shown in **Figure S3b**. We observed that the charge carrier concentration increased linearly with the light intensities for the entire devices as described by the behaviour of charge photogeneration in the bulk [25]. However, the slopes of D1, D4 and D5 were noticeably increased compared to the slopes of D2 and D3. This attitude of D1, D4, and D5 might be attributed to the implemented trap states into the bulk because of the thickness variation which could produce increasing in the hole density in the polymer [25], [59], [64]. In addition, previous research has shown that the photocurrent generated in organic solar cells may be related to the width of the depletion layer in relation to the thickness of the junction [62]. Thus, less charge carrier concentration devices with the fully depletion are showing better performance than the highly charge carrier concentration devices with similar device architecture [65], [66]. That applied in our case where D2 and D3 have the lowest N_{PM6} as well providing better performances among the others. Furthermore, all the fabricated devices showed a fully depletion behavior as previously discussed. These results were excellent agreed with the J-V characteristics of the fabricated NF-OSCs shown the best performance for D2 and D3.

IV. CONCLUSION

This study examined non fullerene organic solar cells with an ITO/PEDOT:PSS/PM6:Y7/PDINO/Ag structure and varying thicknesses of the photoactive layer. The photovoltaic properties and charge carrier recombination behavior of these cells were analyzed using impedance spectroscopy. Through optimization of the photoactive layer thickness, the power conversion efficiency (PCE) of the organic solar cells increased from 15.04% to 17.33%. Impedance

spectroscopy analysis, including Cole-Cole plots, Cf-DOS, and C-V characteristics, provided insight into the recombination contribution, which was less significant for the D2-based devices, depicting their boosting performance.

REFERENCES

[1] G. Li, R. Zhu, and Y. Yang, "Polymer solar cells," *Nat. Photon.*, vol. 6, no. 3, pp. 153–161, 2012.

[2] S. R. Forrest, "The path to ubiquitous and low-cost organic electronic appliances on plastic," *Nature*, vol. 428, no. 6986, pp. 911–918, 2004.

[3] H. K. H. Lee et al., "Organic photovoltaic cells-promising indoor light harvesters for self-sustainable electronics," *J. Mater. Chem. A*, vol. 6, no. 14, pp. 5618–5626, 2018.

[4] A. Facchetti, "Polymer donor-polymer acceptor (all-polymer) solar cells," *Mater. Today*, vol. 16, no. 4, pp. 123–132, 2013.

[5] L. Schmidt-Mende et al., "Self-organized discotic liquid crystals for high-efficiency organic photovoltaics," *Science*, vol. 293, no. 5532, pp. 1119–1122, 2001.

[6] C. R. McNeill and N. C. Greenham, "Conjugated-polymer blends for optoelectronics," *Adv. Mater.*, vol. 21, nos. 38–39, pp. 3840–3850, 2009.

[7] J. Hou, O. Inganas, R. H. Friend, and F. Gao, "Organic solar cells based on non-fullerene acceptors," *Nat. Mater.*, vol. 17, no. 2, pp. 119–128, 2018.

[8] Q. Liu et al., "18% efficiency organic solar cells," *Sci. Bull.*, vol. 65, no. 4, pp. 272–275, 2020.

[9] L. Ma, S. Zhang, J. Wang, Y. Xu, and J. Hou, "Recent advances in non-fullerene organic solar cells: From lab to FAB," *Chem. Commun.*, vol. 56, no. 92, pp. 14337–14352, 2020.

[10] C. Duan, F. Huang, and Y. Cao, "Recent development of push-pull conjugated polymers for bulk-heterojunction photovoltaics: Rational design and fine tailoring of molecular structures," *J. Mater. Chem.*, vol. 22, no. 21, pp. 10416–10434, 2012.

[11] Y. J. Cheng, S. H. Yang, and C. S. Hsu, "Synthesis of conjugated polymers for organic solar cell applications," *Chem. Rev.*, vol. 109, no. 11, pp. 5868–5923, 2009.

[12] C. Yi and X. Gong, "Towards high performance inverted polymer solar cells," *Current Opin. Chem. Eng.*, vol. 2, no. 1, pp. 125–131, 2013.

[13] Y. Li, "Molecular design of photovoltaic materials for polymer solar cells: Toward suitable electronic energy levels and broad absorption," *Accounts Chem. Res.*, vol. 45, no. 5. pp. 723–733, 2012.

[14] Y. Lin et al., "17% efficient organic solar cells based on liquid exfoliated WS$_2$ as a replacement for PEDOT:PSS," *Adv. Mater.*, vol. 31, no. 46, 2019, Art. no. 1902965.

[15] Y. Cui et al., "Over 16% efficiency organic photovoltaic cells enabled by a chlorinated acceptor with increased open-circuit voltages," *Nat. Commun.*, vol. 10, no. 1, pp. 1–8, 2019.

[16] Y. Cui et al., "Organic photovoltaic cell with 17% efficiency and superior processability," *Nat. Sci. Rev.*, vol. 7, no. 7, pp. 1239–1246, 2020.

[17] L. Zhu et al., "Single-junction organic solar cells with over 19% efficiency enabled by a refined double-fibril network morphology," *Nat. Mater.*, vol. 21, no. 6, pp. 656–663, 2022.

[18] J. Liu et al., "Fast charge separation in a non-fullerene organic solar cell with a small driving force," *Nat. Energy*, vol. 1, no. 7, pp. 1–7, 2016.

[19] D. Baran et al., "Reduced voltage losses yield 10% efficient fullerene free organic solar cells with >1 V open circuit voltages," *Energy Environ. Sci.*, vol. 9, no. 12, pp. 3783–3793, 2016.

[20] B. Kan et al., "Fine-Tuning the energy levels of a nonfullerene small-molecule acceptor to achieve a high short-circuit current and a power conversion efficiency over 12% in organic solar cells," *Adv. Mater.*, vol. 30, no. 3, pp. 1–8, 2018.

[21] Y. Li et al., "Non-fullerene acceptor with low energy loss and high external quantum efficiency: Towards high performance polymer solar cells," *J. Mater. Chem. A*, vol. 4, no. 16, pp. 5890–5897, 2016.

[22] X.-K. Chen and J.-L. Brédas, "Voltage losses in organic solar cells: Understanding the contributions of intramolecular vibrations to non-radiative recombinations," *Adv. Energy Mater.*, vol. 8, no. 9, pp. 1–9, 2018.

[23] E. Moustafa, J. G. Sánchez, L. F. Marsal, and J. Pallarès, "Stability enhancement of high-performance inverted polymer solar cells using ZnO electron interfacial layer deposited by intermittent spray pyrolysis approach," *ACS Appl. Energy Mater.*, vol. 4, no. 4, pp. 4099–4111, 2021.

[24] J. G. Sánchez et al., "Impact of inkjet printed ZnO electron transport layer on the characteristics of polymer solar cells," *RSC Adv.*, vol. 8, no. 24, pp. 13094–13102, 2018.

[25] H. F. Haneef, A. M. Zeidell, and O. D. Jurchescu, "Charge carrier traps in organic semiconductors: A review on the underlying physics and impact on electronic devices," *J. Mater. Chem. C*, vol. 8, no. 3, pp. 759–787, 2020.

[26] M. B. Upama et al., "Effect of annealing dependent blend morphology and dielectric properties on the performance and stability of non-fullerene organic solar cells," *Solar Energy Mater. Solar Cells*, vol. 176, pp. 109–118, Mar. 2018.

[27] K. A. O'Hara et al., "Role of crystallization in the morphology of polymer:Non-fullerene acceptor bulk heterojunctions," *ACS Appl. Mater. Interfaces*, vol. 9, no. 22, pp. 19021–19029, 2017.

[28] K. Weng et al., "Optimized active layer morphology toward efficient and polymer batch insensitive organic solar cells," *Nat. Commun.*, vol. 11, no. 1, p. 2855, 2020.

[29] B. Du et al., "Heating induced aggregation in non-fullerene organic solar cells towards high performance," *J. Energy Chem.*, vol. 54, pp. 131–137, Mar. 2021.

[30] E. Moustafa, M. Méndez, J. G. Sánchez, J. Pallarès, E. Palomares, and L. F. Marsal, "Thermal activation of pedot:PSS/PM6:Y7 Based films leads to unprecedent high short-circuit current density in nonfullerene organic photovoltaics," *Adv. Energy Mater.*, vol. 13, no. 4, 2022, Art. no. 2203241.

[31] E. Moustafa, J. Pallarès, and L. F. Marsal, "Revealing the influence of annealing treatment on the performance of non-fullerene organic photovoltaics," in *Proc. 35th Symp. Microelectron. Technol. Devices (SBMicro)*, 2021, pp. 1–4, doi: 10.1109/SBMicro50945.2021.9585750.

[32] G. Zhang et al., "High-performance ternary organic solar cell enabled by a thick active layer containing a liquid crystalline small molecule donor," *J. Amer. Chem. Soc.*, vol. 139, no. 6, pp. 2387–2395, 2017.

[33] J. Yuan et al., "Single-junction organic solar cell with over 15% efficiency using fused-ring acceptor with electron-deficient core," *Joule*, vol. 3, no. 4, pp. 1140–1151, 2019.

[34] E. Moustafa, L. F. Marsal, and J. Pallarès, "Significant stability improvement of fullerene organic photovoltaics via ZnO film modification through the intermittent spray pyrolysis technique," *ACS Appl. Energy Mater.*, vol. 5, no. 4, pp. 4390–4403, 2022.

[35] J. Yao et al., "Cathode engineering with perylene-diimide interlayer enabling over 17% efficiency single-junction organic solar cells," *Nat. Commun.*, vol. 11, no. 1, p. 2726, 2020.

[36] A. M. Peiro et al., "Hybrid polymer/metal oxide solar cells based on ZnO columnar structures," *J. Mater. Chem.*, vol. 16, no. 21, p. 2088, 2006.

[37] E. Moustafa, A. A. A. Torimtubun, J. Pallarès, and L. F. Marsal, "Effect of additives and annealing on the performance of nonfullerene-based binary and ternary organic photovoltaics," *Solar RRL*, vol. 6, no. 1, 2021, Art. no. 2100480.

[38] E. Moustafa, M. Méndez, J. Pallarès, and L. F. Marsal, "Low temperature based PDINO cathode interlayer for high operational photostable inverted non-fullerene organic solar cells," *Solar Energy Mater. Solar Cells*, vol. 248, Dec. 2022, Art. no. 111985.

[39] L. Zhan et al., "Over 17% efficiency ternary organic solar cells enabled by two non-fullerene acceptors working in an alloy-like model," *Energy Environ. Sci.*, vol. 13, no. 2, pp. 635–645, 2020.

[40] B. Qi and J. Wang, "Fill factor in organic solar cells," *Phys. Chem. Chem. Phys.*, vol. 15, no. 23, pp. 8972–8982, 2013.

[41] N. Tokmoldin et al., "Extraordinarily long diffusion length in PM6:Y6 organic solar cells," *J. Mater. Chem. A*, vol. 8, no. 16, pp. 7854–7860, 2020.

[42] A. J. Mouí, J. B. Bonekamp, and K. Meerholz, "The effect of active layer thickness and composition on the performance of bulk-heterojunction solar cells," *J. Appl. Phys.*, vol. 100, no. 9, 2006, Art. no. 94503.

[43] J. Nelson, "Diffusion-limited recombination in polymer-fullerene blends and its influence on photocurrent collection," *Phys. Rev. Amer. Phys. Soc.*, vol. 67, no. 15, pp. 1–10, 2003.

[44] S. Foster et al., "Electron collection as a limit to polymer:PCBM solar cell efficiency: Effect of blend microstructure on carrier mobility and device performance in PTB7:PCBM," *Adv. Energy Mater.*, vol. 4, no. 14, pp. 1–12, 2014.

[45] M. H. Jao, H. C. Liao, and W. F. Su, "Achieving a high fill factor for organic solar cells," *J. Mater. Chem. A*, vol. 4, no. 16, pp. 5784–5801, 2016.

[46] C. M. Proctor and T. Q. Nguyen, "Effect of leakage current and shunt resistance on the light intensity dependence of organic solar cells," *Appl. Phys. Lett.*, vol. 106, no. 8, 2015, Art. no. 83301.

[47] G. A. H. Wetzelaer, M. Kuik, M. Lenes, and P. W. M. Blom, "Origin of the dark-current ideality factor in polymer: Fullerene bulk hetero-junction solar cells," *Appl. Phys. Lett.*, vol. 99, no. 15, pp. 2011–2014, 2011.

[48] C. Hou and H. Yu, "ZnO/Ti$_3$C$_2$Tx monolayer electron transport layers with enhanced conductivity for highly efficient inverted polymer solar cells," *Chem. Eng. J.*, vol. 407, Mar. 2021, Art. no. 127192.

[49] J.-L. Wu et al., "Nanoparticles on the performance of polymer bulk heterojunction solar cells," *ACS Nano*, vol. 5, no. 2, pp. 959–67, 2011.

[50] Z. Liu and N. Wang, "Small energy loss in ternary organic solar cells with a blend of cascade energy levels: Two fullerene-free accep-tors as the electron acceptor," *J. Mater. Chem. C*, vol. 7, no. 32, pp. 10039–10048, 2019.

[51] C. Yang et al., "Effects of energy-level offset between a donor and acceptor on the photovoltaic performance of non-fullerene organic solar cells," *J. Mater. Chem. A*, vol. 7, no. 32, pp. 18889–18897, 2019.

[52] E. Von Hauff, "Impedance spectroscopy for emerging photovoltaics," *J. Phys. Chem. C*, vol. 123, no. 18, pp. 11329–11346, 2019.

[53] A. Abat, M. Méndez, J. G. Sánchez, J. Pallarès, E. Palomares, and L. F. Marsal, "Shelf-life degradation analysis of nonencapsulated organic solar cells via combined dark J-V modeling, impedance and transient spectroscopy techniques," *Sustain. Energy Fuels*, vol. 5, no. 24, pp. 6498–6508, 2021.

[54] E. Osorio et al., "Degradation analysis of encapsulated and nonen-capsulated TiO$_2$/PTB$_7$:PC$_{70}$BM/V$_2$O$_5$ solar cells under ambient conditions via impedance spectroscopy," *ACS Omega*, vol. 2, no. 7, pp. 3091–3097, 2017.

[55] H. Schroeder, "Poole–Frenkel-effect as dominating current mechanism in thin oxide films—An illusion?" *J. Appl. Phys.*, vol. 117, no. 21, 2015, Art. no. 215103.

[56] I. Gelmetti, L. Cabau, N. F. Montcada, and E. Palomares, "Selective organic contacts for methyl ammonium lead iodide (MAPI) per-ovskite solar cells: Influence of layer thickness on carriers extraction and carriers lifetime," *ACS Appl. Mater. Interfaces*, vol. 9, no. 26, pp. 21599–21605, 2017.

[57] S. S. Hegedus and E. A. Fagen, "Midgap states in a-Si:H and a-SiGe:H p-i-n solar cells and Schottky junctions by capacitance techniques," *J. Appl. Phys.*, vol. 71, no. 12, pp. 5941–5951, 1992.

[58] S. Wang, P. Kaienburg, B. Klingebiel, D. Schillings, and T. Kirchartz, "Understanding thermal admittance spectroscopy in low-mobility semiconductors," *J. Phys. Chem. C*, vol. 122, no. 18, pp. 9795–9803, 2018.

[59] B. Ecker et al., "Degradation effects related to the hole transport layer in organic solar cells," *Adv. Funct. Mater.*, vol. 21, no. 14, pp. 2705–2711, 2011.

[60] T. Walter, R. Herberholz, C. Müller, and H. W. Schock, "Determination of defect distributions from admittance measurements and application to Cu(In,Ga)Se$_2$ based heterojunctions," *J. Appl. Phys.*, vol. 80, no. 8, pp. 4411–4420, 1996.

[61] J. Bhattacharya, P. H. Joshi, R. Biswas, and V. L. Dalal, "Pathway for recovery of photo-degraded polymer solar cells by post degradation thermal anneal," *Solar Energy Mater. Solar Cells*, vol. 164, pp. 70–79, May 2017.

[62] J. Wu et al., "Tail state limited photocurrent collection of thick pho-toactive layers in organic solar cells," *Nat. Commun.*, vol. 10, no. 1, p. 5159, 2019.

[63] J. C. Nolasco et al., "Relation between the barrier interface and the built-in potential in pentacene/C$_{60}$ solar cell," *Appl. Phys. Lett.*, vol. 97, no. 1, 2010, Art. no. 013305.

[64] A. Seemann, H. J. Egelhaaf, C. J. Brabec, and J. A. Hauch, "Influence of oxygen on semi-transparent organic solar cells with gas permeable electrodes," *Org. Electron.*, vol. 10, no. 8, pp. 1424–1428, 2009.

[65] S. Dahlström et al., "Extraction current transients for selective charge-carrier mobility determination in non-fullerene and ternary bulk heterojunction organic solar cells," *ACS Appl. Energy Mater.*, vol. 3, no. 9, pp. 9190–9197, 2020.

[66] T. Kirchartz, T. Agostinelli, M. Campoy-Quiles, W. Gong, and J. Nelson, "Understanding the thickness-dependent performance of organic bulk heterojunction solar cells: The influence of mobility, lifetime, and space charge," *J. Phys. Chem. Lett.*, vol. 3, no. 23, pp. 3470–3475, 2012.